

ARTICLE OPEN



First-principles theory of extending the spin qubit coherence time in hexagonal boron nitride

Jaewook Lee¹, Huijin Park¹ and Hosung Seo¹✉

Negatively charged boron vacancies (V_B^-) in hexagonal boron nitride (h-BN) are a rapidly developing qubit platform in two-dimensional materials for solid-state quantum applications. However, their spin coherence time (T_2) is very short, limited to a few microseconds owing to the inherently dense nuclear spin bath of the h-BN host. As the coherence time is one of the most fundamental properties of spin qubits, the short T_2 time of V_B^- could significantly limit its potential as a promising spin qubit candidate. In this study, we theoretically proposed two materials engineering methods, which can substantially extend the T_2 time of the V_B^- spin by four times more than its intrinsic T_2 . We performed quantum many-body computations by combining density functional theory and cluster correlation expansion and showed that replacing all the boron atoms in h-BN with the ^{10}B isotope leads to the coherence enhancement of the V_B^- spin by a factor of three. In addition, the T_2 time of the V_B^- can be enhanced by a factor of 1.3 by inducing a curvature around V_B^- . Herein, we elucidate that the curvature-induced inhomogeneous strain creates spatially varying quadrupole nuclear interactions, which effectively suppress the nuclear spin flip-flop dynamics in the bath. Importantly, we find that the combination of isotopic enrichment and strain engineering can maximize the T_2 time of V_B^- , yielding 207.2 μs and 161.9 μs for single- and multi-layer h- ^{10}BN , respectively. Furthermore, our results can be applied to any spin qubit in h-BN, strengthening their potential as material platforms to realize high-precision quantum sensors, quantum spin registers, and atomically thin quantum magnets.

npj 2D Materials and Applications (2022)6:60; <https://doi.org/10.1038/s41699-022-00336-2>

INTRODUCTION

Optically addressable spin defects in wide band-gap materials are promising solid-state qubit platforms that enable cutting-edge quantum applications such as quantum computation¹, quantum sensing², and quantum network^{3,4}. Spin defects in diamond⁵, which show long spin coherence times and many other attractive features such as high-temperature quantum functionality⁶ and spin-to-photon interfaces⁷, is one of the leading qubit systems for quantum applications. Progresses made in the research on diamond have inspired several pioneering studies, wherein quantum spin defects have been developed in silicon carbide and nitrides, broadening the palette of spin qubits in materials^{8–11}. Notably, the spin qubits in non-diamond hosts provide unique opportunities for building advanced platforms for quantum systems by taking advantage of the well-established material technologies developed for their hosts^{12,13}. Recently, the search for qubit systems in two-dimensional (2D) van der Waals (vdW) materials has gained significant attention owing to their potential superiority in light extraction, heterostructuring, defect positioning, strain engineering, and nano-photonics integration^{14–17}.

Among the 2D vdW materials, quantum spin defects in hexagonal boron nitride (h-BN) are gaining prominence for the development of optically active spin qubits. Owing to its wide bandgap of ~ 6 eV, h-BN hosts a variety of color centers from near infrared to ultraviolet^{15,16,18}. Some of the color centers have been found to emit bright single photons even at room temperature, and these findings have sparked worldwide research efforts in this direction^{19–25}. Subsequently, the search for optically addressable spin qubits in h-BN has become the focus of materials research, and several breakthroughs have been made recently. Notably, negatively charged boron vacancies (V_B^-) were discovered as

optically addressable spin qubits in h-BN^{26–28}. Since the first report by Gottscholl et al.²⁶, several important achievements have been made²⁹, including the realization of coherent Rabi oscillations³⁰, deterministic defect generations^{31–33}, nano-scale quantum sensing³⁴, and coupling to nano-photonics structures³⁵. In addition, carbon-related defects^{36–38} and boron vacancy complexes have also been recently identified as optically accessible spin qubits in h-BN. Overall, significant advances have been made in the development of defect-based spin qubits in h-BN and their use in quantum applications. Nonetheless, further research is required to realize robust spin qubits in h-BN.

One of the most compelling issues for h-BN spin qubits is their short spin coherence time (T_2) due to the dense nuclear spin bath in the h-BN lattice^{26,39}. For V_B^- , the Hahn-echo T_2 time has been measured to be several microseconds³⁰. Notably, several well-known schemes, such as isotopic purification⁴⁰, dynamical decoupling (DD)⁴¹, and clock transitions (CT)^{42,43}, are available to extend the spin coherence times in materials. However, in h-BN, a conventional isotopic purification is impossible because all the naturally occurring boron (^{10}B and ^{11}B) and nitrogen (^{14}N and ^{15}N) isotopes exhibit non-zero nuclear spins. In addition, the coherence protection schemes such as DD and CT are often limited by the intrinsic Hahn-echo T_2 time. When the T_2 time is extremely short like in h-BN, pulse requirements in the DD and CT schemes become considerably challenging¹¹. Considering the fundamental role of the coherence time in determining the retention time of the quantum information, the short T_2 time of the h-BN spin qubits is one of the most pressing problems that needs to be solved for advancing these platforms in h-BN.

In this study, by taking the V_B^- spin as a representative spin qubit system in h-BN, we developed two unconventional methods to enhance the T_2 time of spin qubits significantly in h-BN via

¹Department of Physics and Department of Energy Systems Research, Ajou University, Suwon, Gyeonggi 16499, Korea. ✉email: hseo2017@ajou.ac.kr

isotopic enrichment and strain engineering. We combined density functional theory (DFT) and cluster correlation expansion (CCE) to compute the theoretical T_2 time of V_B^- in h-BN single layer and multiple layers to be $45.9\ \mu\text{s}$ and $26.6\ \mu\text{s}$, respectively, in the presence of an intrinsic nuclear spin bath in natural h-BN. Subsequently, we showed that the T_2 times were increased to 143.4 and $81.1\ \mu\text{s}$ in the single- and multi-layer $h\text{-}^{10}\text{B}$ N, respectively, which is enriched with the ^{10}B isotope. This result is somewhat counterintuitive as the ^{10}B isotope has a larger nuclear spin ($I=3$) than that of the ^{11}B isotope ($I=3/2$). We found that this T_2 enhancement by a factor of three resulted from the smaller gyromagnetic ratio of ^{10}B than that of ^{11}B , despite the much larger nuclear spin of ^{10}B . In addition, we demonstrated that the T_2 time could be further increased to $207.2\ \mu\text{s}$ and $161.9\ \mu\text{s}$ for the single- and multi-layer $h\text{-}^{10}\text{B}$ N, respectively, by inducing inhomogeneous strain around the V_B^- . We considered a Gaussian-shaped bubble around V_B^- as a representative inhomogeneous strain and showed that the T_2 increased in proportion to the Gaussian width and height, demonstrating the impact of the local inhomogeneous strain on the T_2 time. We found that a spatial inhomogeneity in the nuclear spin quadrupole interaction effect, induced by the inhomogeneous strain, plays a crucial role in suppressing the nuclear spin flip-flop dynamics, thus enhancing the V_B^- spin coherence. Our results pave the way for effective protection of the spin coherence in h-BN, and this method should be applicable to V_B^- as well as to any potential spin qubits in h-BN^{44,45}. Improved spin coherence of V_B^- would also open possibilities of further coherence extension using DD or CT, thereby advancing spin qubits in h-BN as promising platforms for quantum information science and technology.

RESULTS

Spin decoherence of V_B^- in natural h-BN

We considered a central spin model to compute the decoherence dynamics of a V_B^- spin interacting with the nuclear spin bath in the h-BN lattice. Figure 1a shows a schematic of the spin model, in which a V_B^- defect is created in the middle of a large h-BN supercell. The ground state of V_B^- is a spin-triplet state, and the spin density is highly localized at the vacancy site (see inset of Fig. 1a). In our model, we assumed a localized $S=1$ at the vacancy site and treated its $+1$ and 0 spin sublevels as qubit states. The nuclear spin bath, which strongly interacts with the V_B^- spin via hyperfine interaction, is derived from the spin-bearing boron and nitrogen nuclei in h-BN. Notably, all the naturally occurring boron and nitrogen isotopes exhibit non-zero nuclear spins: 19.9% of ^{10}B with $I=3$, 80.1% of ^{11}B with $I=3/2$, 99.6% of ^{14}N with $I=1$, and 0.4% of ^{15}N with $I=1/2$. In our model, we randomly distributed the nuclear spins in the h-BN lattice according to their natural abundance. To compute the homogeneous dephasing time (T_2) of the V_B^- spin, we considered the Hahn-echo pulse sequence⁴⁶ and used the CCE method to expand the many-body nuclear-spin correlation effects systematically on the V_B^- spin decoherence⁴⁷. Notably, the CCE method combined with DFT calculations enables the quantum many-body computation of T_2 without the assumption of any adjustable theoretical parameter. Owing to its predictive power, the CCE method was successfully applied to a wide range of solid-state qubit systems, yielding excellent agreement with the experimental results^{11,48–52} (further details on the theoretical methods and the system's spin Hamiltonian are provided in the Method and Supplementary Information sections; see Supplementary Note 1 and 2, and Supplementary Fig. 1).

Figure 1b presents the computed spin coherence of V_B^- in the bulk of natural h-BN. Evidently, the spin coherence rapidly decays during the free evolution time, within tens of microseconds. By fitting the coherence with a stretched exponential function ($\exp(-t_{\text{free}}/T_2)^n$), we computed the T_2 time and stretching

exponent (n) of the decay to be $26.64\ \mu\text{s}$ and 2.64 , respectively. In addition, we determined T_2 and n of the V_B^- spin in the single-layer h-BN to be $45.85\ \mu\text{s}$ and 2.27 , respectively, owing to the reduced number of nuclear spins surrounding V_B^- (see Supplementary Fig. 2). Notably, the computed T_2 time corresponds to the upper limit of T_2 set by the intrinsic nuclear spin bath of h-BN. The experimentally measured T_2 time can be smaller than the theoretical T_2 ³⁰, if other decoherence sources such as other paramagnetic defects are present in h-BN.

To examine the nuclear bath dynamics generating the intracrystalline magnetic noise, we analyzed the impact of the spin Hamiltonian terms on the V_B^- spin decoherence. Importantly, we find that the nuclear quadrupole interaction⁵³ plays an important role in determining the bath dynamics in h-BN. Figure 1b shows the V_B^- decoherence computed with a partial spin Hamiltonian, in which the quadrupole Hamiltonian terms are excluded from the model. We observe that the spin coherence decays much faster in the “without-the-quadrupole” model than in the “with-the-quadrupole” model. Without the quadrupole interaction effect in the model, the T_2 time of V_B^- is reduced to $17.92\ \mu\text{s}$ and $34.98\ \mu\text{s}$ for the multi- and single-layer h-BN, respectively³⁹. Notably, the nuclear spin flip-flop transitions, driven by the magnetic dipolar coupling between the nuclear spins, are the dominant sources of intracrystalline magnetic noise in a nuclear spin bath^{48,52,54}. Our results show that the nuclear quadrupole interaction in h-BN plays a significant role in suppressing such nuclear flip-flop transitions in the h-BN.

To understand the role of quadrupole interaction in the pairwise nuclear spin transitions, we show the energy levels of two ^{10}B nuclear spins, defined as $|m_1, m_2\rangle$, where $m_i = 3, 2, 1, 0, -1, -2, -3$, in Fig. 1c–e. Figure 1c shows the energy level splitting due to the Zeeman interaction (H_Z) and hyperfine field imposed by the V_B^- spin (H_{Hyper}). The Zeeman splitting yields spin manifolds, which are separated from each other in energy by $13.7\ \text{MHz}$ in the presence of an external magnetic field of $3\ \text{T}$. Each manifold contains certain number of two-spin states such as $\{|-3, -1\rangle, |-2, -2\rangle, |-1, -3\rangle\}$, which have the same Zeeman energy, as shown in Fig. 1d. These states in a manifold are split by a small energy of the order of hundreds of Hz because of the hyperfine field (denoted as Δ_{HF} in Fig. 1d). In the “without-the-quadrupole” decoherence model, the magnetic dipolar interaction drives the flip-flop transitions between the states, confined in each manifold, with a transition rate of hundreds of Hz (denoted as Ω_{FF} in Fig. 1d). However, the transitions are strongly suppressed between the states belonging to different manifolds because of a large Zeeman energy mismatch. Remarkably, the energy levels in a manifold exhibit significant splitting in the presence of the quadrupole interaction, as shown in Fig. 1e. We found that the quadrupole-induced splitting ($\Delta_{\text{HF}+Q}$ in Fig. 1e) ranges from tens of kHz to a few MHz, owing to the large nuclear quadrupole interaction in h-BN (see Table 1). Thus, the flip-flop transitions within a Zeeman manifold are significantly suppressed, compared to those evaluated using the “without-the-quadrupole” model, because of the large quadrupole-driven energy mismatch. Our analysis reveals the importance of the quadrupole interaction in determining the nuclear bath dynamics, which in turn governs the spin decoherence of the spin qubits in h-BN.

Isotopic enrichment of h-BN to increase T_2

Figure 2 depicts the computed T_2 of V_B^- in h-BN as a function of the composition ratio of ^{10}B and ^{14}N in h-BN. Surprisingly, we find that the T_2 time substantially increases as the ratio of ^{10}B and ^{14}N increases toward 100% in the lattice, despite their larger nuclear spins than those of ^{11}B and ^{15}N . When h-BN is 100% enriched with ^{10}B and ^{14}N (i.e., $h\text{-}^{10}\text{B}^{14}\text{N}$), the T_2 time is increased to $143.39\ \mu\text{s}$ and $81.11\ \mu\text{s}$ in the single- and multi-layer $h\text{-}^{10}\text{B}^{14}\text{N}$, respectively. These values are three times larger than those in natural h-BN.

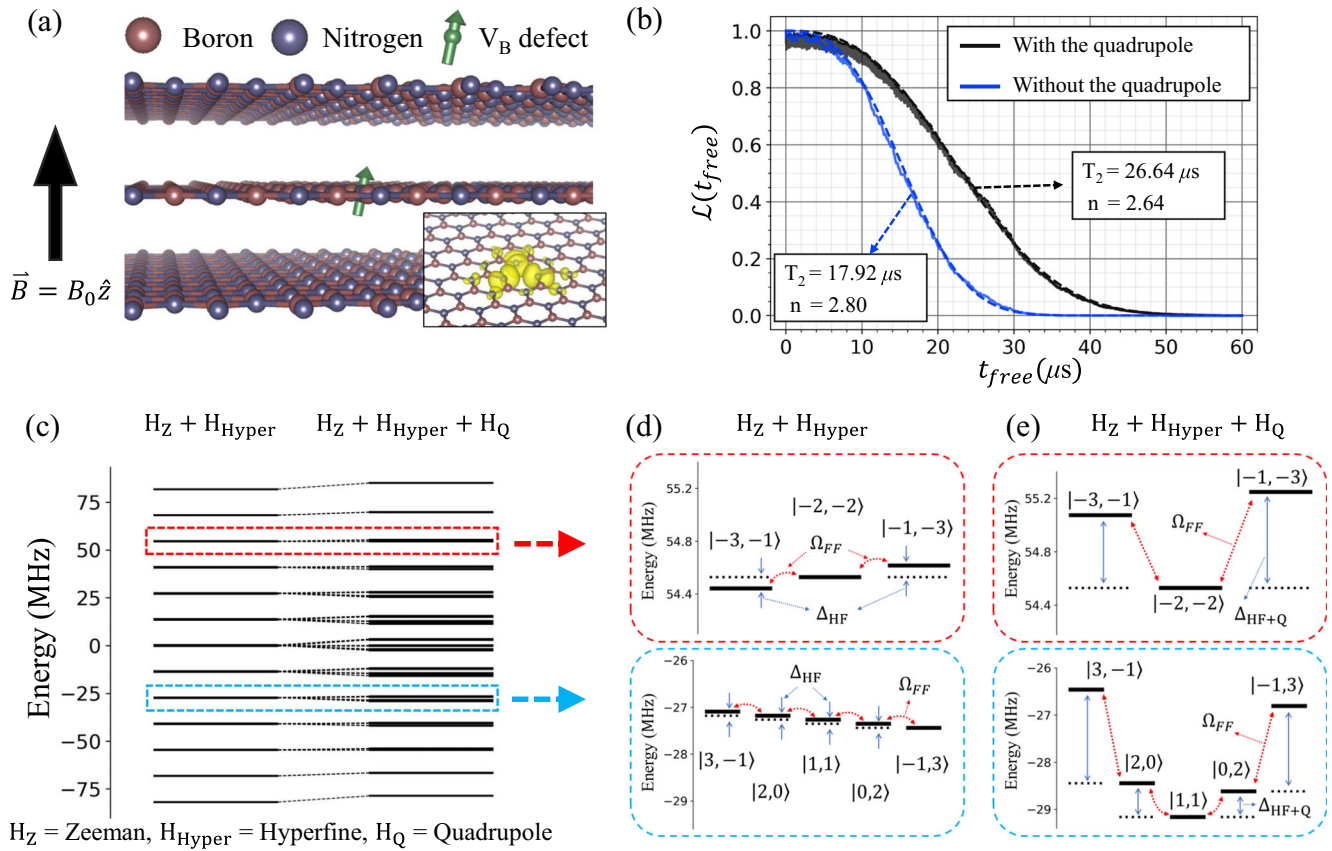


Fig. 1 Spin decoherence of V_B^- in bulk h-BN. **a** Schematic of the V_B^- spin in multi-layer h-BN. An external magnetic field (B_0) of 3 T is applied along the out-of-plane direction. Inset shows the ground-state spin density of V_B^- , computed using DFT. **b** Spin coherence of the V_B^- spin in multi-layer h-BN (black line). The spin coherence is fitted with a stretched exponential function, $\exp(-t_{free}/T_2)^n$, to compute the spin coherence time (T_2) and stretching exponent (n). A hypothetical model of the bath in which the nuclear quadrupole interaction is ignored was considered for comparison (blue line). **c** Energy levels of two ^{10}B nuclear spins in the presence of Zeeman effect (H_Z) and a hyperfine field (H_{Hyper}) imposed by the V_B^- electron spin (left) and in the presence of H_Z , H_{Hyper} , and the nuclear quadrupole interaction (H_Q) (right). **d, e** Detailed energy-level diagrams for the two specific manifolds, denoted by the red and blue dotted lines in (c), (d) in the presence of H_Z and H_{Hyper} and (e) in the presence of H_Z , H_{Hyper} , and H_Q . For a given manifold, transitions allowed by the dipolar flip-flop interactions are denoted by red dotted arrows, and their transition rates are indicated as Ω_{FF} . The energy splitting between the states in (d) is only induced by a small hyperfine field (denoted as Δ_{HF}), whereas it is given by both the hyperfine and quadrupole interactions (denoted as Δ_{HF+Q}).

Table 1. Electric field gradients in h-BN, and the corresponding quadrupole coupling constants (eQV_{zz}) computed using DFT.

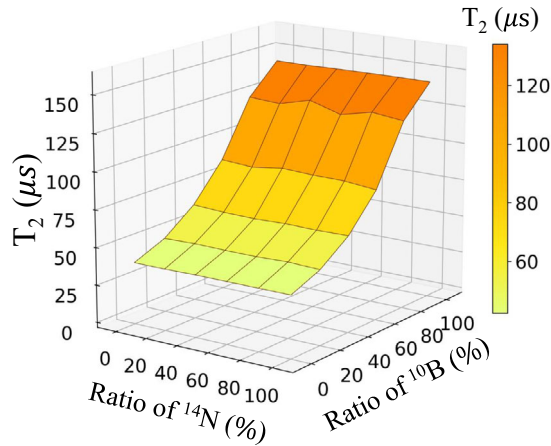
Isotopes	$V_{xx} = V_{yy}$ (eV/Å ²)	V_{zz} (eV/Å ²)	eQV_{zz} (MHz)	eQV_{zz} (Exp. ⁶⁸) (MHz)
^{10}B	-15.450	30.901	6.260	6.1
^{11}B	-15.450	30.901	3.004	2.9
^{14}N	-2.478	4.956	0.23	0.2

In contrast, the T_2 times in single- and multi-layer h- ^{11}B are 45.85 μs and 26.64 μs , respectively, which are unanticipated, because a smaller nuclear spin (e.g., $l = 3/2$ of ^{11}B vs. $l = 3$ of ^{10}B) results in a smaller number of flip-flop transition channels in the nuclear spin-spin interaction as well as lower intracrystalline noise in h- $^{11}\text{B}^{15}\text{N}$ than in h- $^{10}\text{B}^{14}\text{N}$. However, our results show that the opposite is true—the intracrystalline magnetic noise is significantly reduced in h- $^{10}\text{B}^{14}\text{N}$.

To elucidate the microscopic origin of the enhanced T_2 in h- $^{10}\text{B}^{14}\text{N}$, we consider a hypothetical central spin model, wherein the gyromagnetic ratio (γ_B) and the nuclear spin number (I_B) at the boron sites are variable. Figure 3 shows T_2 as a function of γ_B and I_B . Considering the actual I_B and γ_B of ^{10}B and ^{11}B (2.875 $\text{rad G}^{-1} \text{ms}^{-1}$ and 8.585 $\text{rad G}^{-1} \text{ms}^{-1}$,

respectively), we consider the range of γ_B to be from 1 to 10 $\text{rad G}^{-1} \text{ms}^{-1}$, and that of I_B from $1/2$ to 3 in Fig. 3. We find that for a given γ_B , the T_2 time decreases as I_B increases, indicating that the intracrystalline magnetic noise increases as the total number of nuclear spin flip-flop channels in the bath (proportional to $(2I_B)^2$) increases. In addition, T_2 increases quadratically as γ_B decreases. For instance, for $I_B = 3/2$, the T_2 changes from 24 μs to 695 μs when γ_B changes from 10 to 1 $\text{rad G}^{-1} \text{ms}^{-1}$. The γ_B -dependent change in T_2 observed mainly because the magnetic dipolar coupling strength is proportional to $(\gamma_B)^2$. Thus, decreasing γ_B reduces the flip-flop transition rate quadratically in the nuclear spin bath. In h- ^{10}B , the total number of flip-flop transitions is increased by four times, but the flip-flop transition rate is substantially decreased by approximately nine times compared to those in h- ^{11}B . In the case of ^{14}N isotope, the same analysis yields four times larger number of flip-flop transition channels and approximately two times smaller flip-flop transition rates in h- ^{14}N compared to those in h- ^{15}N . Therefore, based on the result shown in Fig. 3, we can conclude that in h-BN, the spin coherence of V_B^- is much more sensitive to the change in γ_B than that in I_B , and the increased T_2 in h- $^{10}\text{B}^{14}\text{N}$ stems from the smaller γ_B of the ^{10}B and ^{14}N nuclear spins despite their large nuclear spin numbers.

(a) Single-layer h-BN



(b) Multi-layer h-BN

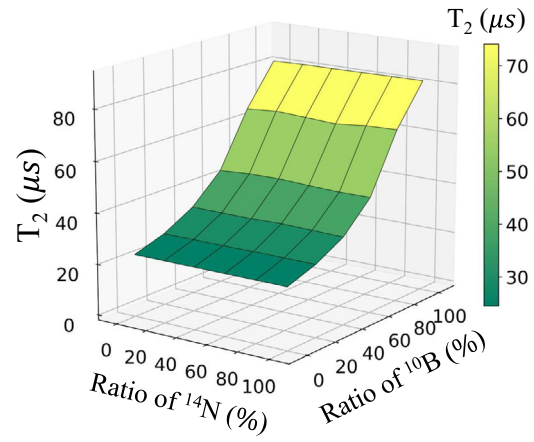


Fig. 2 Enhancement of T_2 in h-BN via isotopic engineering. **a, b** Computed T_2 of the V_B^- spin in **a** monolayer h-BN and **b** multi-layer h-BN as a function of the ratio of ^{14}N and ^{10}B nuclei in the lattice. An external magnetic field of 3 T is applied. The maximum T_2 time is obtained when h-BN is 100% enriched with ^{10}B both in the single- and multi-layer configurations, yielding a T_2 of 143 μs and 81 μs , respectively.

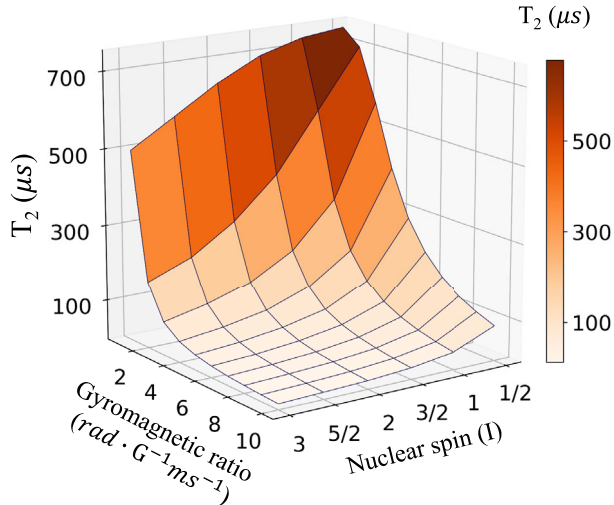


Fig. 3 Hypothetical T_2 of V_B^- in h-BN. Computed T_2 as a function of the gyromagnetic ratio and nuclear spin number of ^{10}B in $h\text{-}^{10}\text{B}^{14}\text{N}$. An external magnetic field of 3 T is applied.

Effects of inhomogeneous lattice strain on spin coherence

Next, we investigate the impact of inhomogeneous lattice strain on the T_2 of V_B^- spin in h-BN. We consider a curved h-BN to create an inhomogeneous strain around V_B^- . Reportedly, various feasible methods have been developed to study the curvature-induced phenomena in h-BN by creating bubbles^{56,57}, pillars³³, folds⁵⁸, and wrinkles²⁰. As a representative model of the local curvature and inhomogeneous strain, we consider a Gaussian lattice deformation as illustrated in Fig. 4a. The lattice deformation can be described in terms of the full width at half maximum (FWHM) and height of the Gaussian function, and the V_B^- defect is created on top of the Gaussian deformation. To cross-check the dependence of our results on the shape of lattice deformation, we also considered two other types of lattice deformations, which are Lorentzian-shape and pillar-shape deformations (see Supplementary Fig. 3). We employed DFT to compute the spin Hamiltonian parameters in the deformed h-BN lattice. The computed effects were subsequently included into the spin Hamiltonian to examine the effect of the inhomogeneous lattice strain on the spin coherence of V_B^- .

Figure 4b shows the computed T_2 time of the V_B^- in natural h-BN (no isotopic modification) as a function of the FWHM and height of the Gaussian lattice deformation. Evidently, the T_2 time increases significantly with the increasing function height and FWHM. At a Gaussian height of 3.5 Å, the T_2 in the single- and multi-layer h-BN is 58.7 μs and 34.2 μs , respectively, as shown in Fig. 4b, c. These values are 12.9 μs and 7.5 μs greater than those in natural and flat h-BN. In Supplementary Fig. 4, we computed the V_B^- spin decoherence in the presence of the Lorentzian-shape and pillar-shape lattice deformations. We found that the V_B^- spin coherence is consistently enhanced in these situations: when the deformation height is 3.5 Å, the T_2 time in the single-layer h-BN reaches 54.6 μs and 72.2 μs in the presence of the Lorentzian- and the pillar-shape deformations, respectively. This result shows that the T_2 enhancement due to inhomogeneous strain is valid regardless of lattice deformation shapes.

To understand the curvature-induced enhancement of the T_2 time, we analyze the impact of the lattice deformation on the V_B^- spin decoherence in terms of two factors: modification of the nuclear spin–spin distances and spatial inhomogeneity induced in the nuclear spin quadrupole interaction in the deformed h-BN lattice. In Supplementary Fig. 6, we consider a model that does not include the nuclear spin quadrupole interaction, and compute T_2 as a function of FWHM and function height same as before (Fig. 4). We find that the T_2 time shows negligible changes, as shown in Supplementary Fig. 6, implying that the enhanced V_B^- spin coherence, obtained using the Gaussian lattice deformation, is not derived from the mere modification of the nuclear spin–spin distances; instead, it is mediated by the modified nuclear quadrupole interaction produced by the inhomogeneous strain.

To visualize the role of nuclear quadrupole interaction in determining the strain-driven enhancement of T_2 , we compute the first-order quadrupole-interaction-induced energy shift (ζ) of a nuclear spin in h-BN. As described in Supplementary Note 3, the energy shift is calculated as: $Q_C \times \zeta \times (3m_l^2 - I(I+1))$, where Q_C is the coefficient of quadrupole interaction (6), and $\zeta = V_{zz} - (V_{xx} + V_{yy})/2$, where V_{ii} ($i = x, y, z$) is the electric field gradient computed using DFT. Figure 5a–c shows ζ as a function of position with respect to the V_B^- site, indicating that a difference of ζ between two different points, shown in Fig. 5a–c, is proportional to the difference between the quadrupole-induced energy shifts of the two nuclear spins at these two different points. As shown in Fig. 5a–c, the inhomogeneity of ζ becomes broader and larger as the Gaussian lattice deformation increases. In Supplementary Fig. 7, we also show

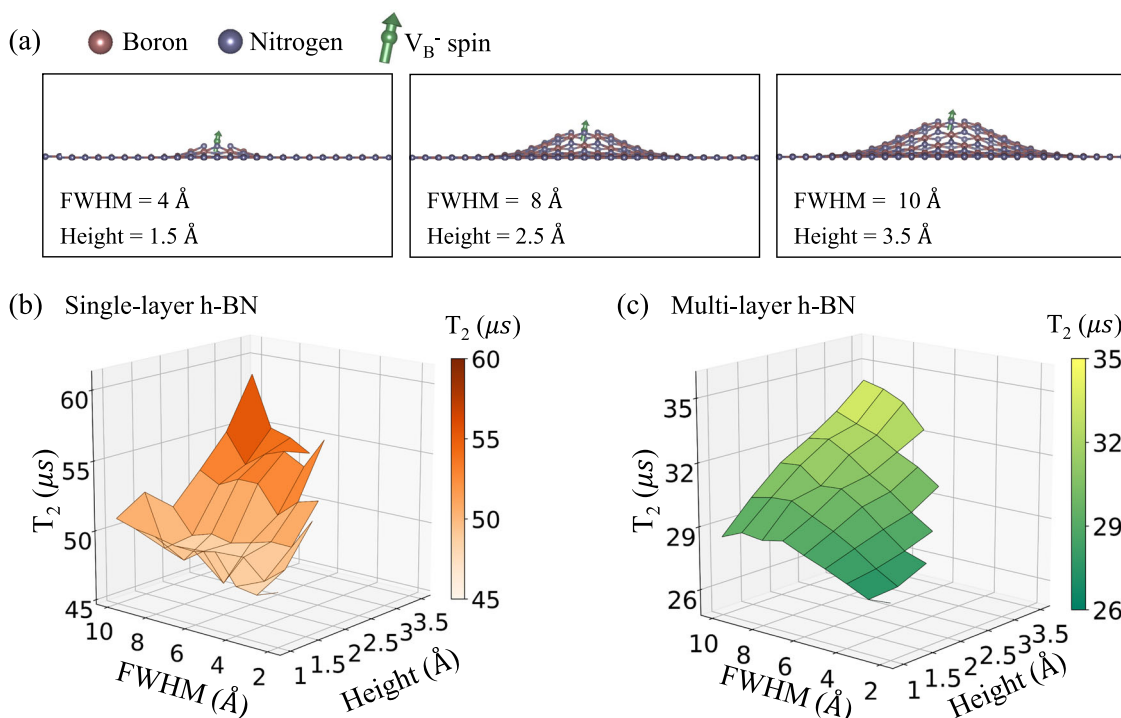


Fig. 4 Strain-induced increase in the T_2 time of V_B^- . **a** Gaussian-shaped lattice deformation of h-BN to induce an inhomogeneous strain around the V_B^- . To control the degree of the lattice deformation, the height (Z) and FWHM of the Gaussian function are varied. **b, c** Computed T_2 times of the V_B^- spin in **(b)** single-layer and **(c)** multi-layer h-BN as functions of the FWHM and height of the Gaussian lattice-deformation function. An external magnetic field of 3 T is applied.

the quadrupole coupling constant ($C_q = eQV_{zz}/\hbar$) and the asymmetry parameter ($\eta_{as} = (V_{xx} - V_{yy})/V_{zz}$) in the presence of the lattice deformation. In terms of the ^{10}B - ^{10}B two-spin energy levels presented in Fig. 1e, a larger difference of ζ between two ^{10}B spins results in a larger level splitting in their two-spin energy levels.

Nuclear spin flip-flop transitions are well understood in terms of a pseudospin model^{48,52}, which can model a flip-flop transition between any two ^{10}B - ^{10}B nuclear spin states having the same Zeeman energy. The two states of a pseudospin are separated by an energy gap (Δ), and the transition between them is mediated by the magnetic dipolar interaction with a flip-flop transition rate (Ω) (see Supplementary Note 4). Figure 5d, e shows the histogram of $(\log(\Omega/\Delta))$ for all the possible pseudospins in the Gaussian-deformed h-BN. Notably, a small $\log(\Omega/\Delta)$ indicates a high suppression in the flip-flop transition. Furthermore, a large Gaussian deformation around the V_B^- defect produces a large number of pseudospins with small $\log(\Omega/\Delta)$ values appearing in the histogram. Our results demonstrate that the energy gap between numerous ^{10}B - ^{10}B pseudospins in h-BN increases as the Gaussian lattice deformation becomes larger, which in turn produces a larger inhomogeneous strain around V_B^- . This results in a considerable suppression of the nuclear flip-flop transitions in h-BN, leading to the enhancement of the T_2 time of V_B^- .

Maximizing the spin coherence time

The two methods suggested in this study can be combined to maximize the T_2 time. Figure 6a, b presents the computed T_2 as a function of the Gaussian height and FWHM for the V_B^- in the Gaussian-deformed $h\text{-}^{10}\text{B}^{14}\text{N}$. Evidently, the maximum achievable T_2 is 207.17 μs and 161.92 μs in the single- (Fig. 6c) and multi-layer h-BN (Fig. 6d), respectively. These values are approximately six times larger than that in natural and flat h-BN. Supplementary Fig. 5 shows the V_B^- spin decoherence in the Lorentzian-deformed single-layer $h\text{-}^{10}\text{B}^{14}\text{N}$ and in the presence of pillar-shape lattice deformation as well. We found that T_2 time reaches 188.9 μs and

308.4 μs for the Lorentzian- and the pillar-shape deformation, respectively, in the single-layer $h\text{-}^{10}\text{B}^{14}\text{N}$. We remark that the combined effect of the smaller gyromagnetic ratio of ^{10}B and the inhomogeneous quadrupole interaction induced by the inhomogeneous strain leads to the enhancement of T_2 of the V_B^- spin.

DISCUSSION

In summary, we proposed two theoretically effective methods to extend the spin coherence time of the V_B^- spin qubit in h-BN. The spin coherence time is otherwise limited to a few microseconds because of the strong intracrystalline magnetic noise caused by the dense nuclear spin bath in the h-BN lattice. To predict the T_2 time of the spin qubit accurately, we performed first-principles calculations by combining the DFT and CCE theory. In a natural h-BN host, the theoretical upper limit of the V_B^- T_2 time is 45.85 μs and 26.64 μs in single- and multi-layer h-BN, respectively. Next, we demonstrated that the T_2 time can be increased to 143.39 μs and 81.11 μs in single- and multi-layer $h\text{-}^{10}\text{B}^{14}\text{N}$, respectively, in which all the boron atoms in the lattice are replaced by the ^{10}B isotope. It is evident that such an isotopic enrichment technique has been already developed and applied to h-BN^{59,60}. By analyzing the magnetic dipolar interaction between the boron nuclear spins, we showed that the smaller gyromagnetic ratio of ^{10}B plays a key role in suppressing the nuclear flip-flop dynamics, despite its large nuclear spin compared to that of ^{11}B . Then, we showed that the T_2 time of V_B^- can be further increased by introducing an inhomogeneous strain around the V_B^- defect. Applying a Gaussian-type lattice deformation (as a representative model of the inhomogeneous strain), we identified that the inhomogeneous strain contributes to the suppression of the nuclear spin flip-flop dynamics in the bath by producing spatially varying nuclear quadrupole interactions in h-BN. We found that applying both the isotopic enrichment and inhomogeneous strain could increase the T_2 time of V_B^- by six times that in a pristine h-BN

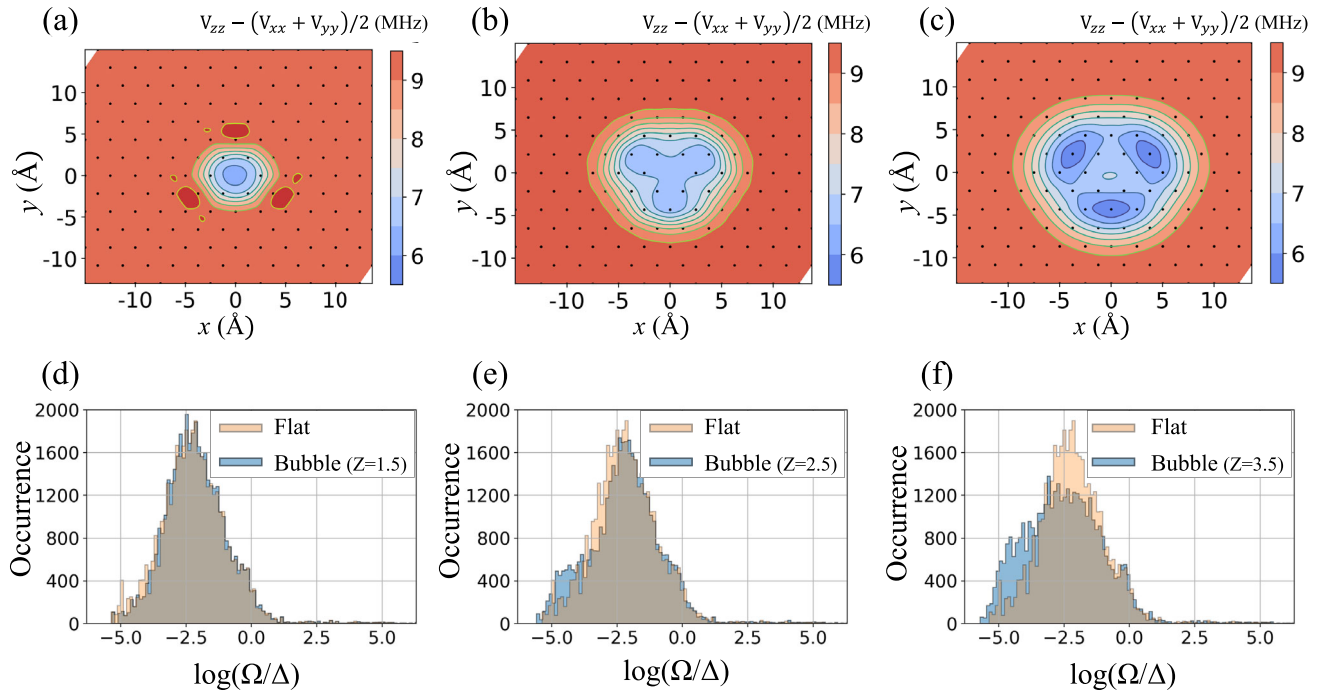


Fig. 5 Inhomogeneous nuclear quadrupole interaction of ^{10}B , induced by an inhomogeneous strain. **a–c** Spatial map of the coefficient of first-order energy shift of the nuclear spins in curved h-BN, due to the quadrupole interaction, which is defined as $\zeta = V_{zz} - (V_{xx} + V_{yy})/2$. Gaussian deformation is applied around the V_{B^-} , and the structures used for **(a)**, **(b)**, and **(c)** are the same as those shown in Fig. 4a, characterized by **a** $Z = 1.5 \text{ \AA}$ and FWHW = 4 \AA , **b** $Z = 2.5 \text{ \AA}$ and FWHW = 8 \AA , and **c** $Z = 3.5 \text{ \AA}$ and FWHW = 10 \AA . **e, f** Histogram of $\log(\Omega/\Delta)$ of all the possible pseudospins in h-BN with Gaussian lattice deformation, where Ω is the flip-flop transition rate, and Δ is the energy gap of a pseudospin (see Supplementary Note 4). The h-BN structures used are characterized by **d** $Z = 3.5 \text{ \AA}$ and FWHW = 10 \AA , **e** $Z = 1.5 \text{ \AA}$ and FWHW = 4 \AA , and **f** $Z = 2.5 \text{ \AA}$ and FWHW = 8 \AA , which are schematically shown in Fig. 4a.

bulk, and consequently, the T_2 can reach up to $207.17 \mu\text{s}$ and $161.92 \mu\text{s}$ for the single- and multi-layer h-BN, respectively.

Our study on V_{B^-} not only provides a fundamental understanding of the decoherence of V_{B^-} spins in h-BN but paves the way to engineer their T_2 times. With an increased T_2 time, the V_{B^-} spin coherence could be further enhanced by combining other active quantum control schemes such as DD or CTs. In addition, the essential physics developed in this study can be applied to any localized spin in any 2D vdW material. Thus, the proposed approach provides a universal tool for engineering the coherence of potential spin qubits in 2D vdW materials. Combining these engineering schemes with the unique characteristics of 2D vdW materials would be a promising strategy for the development of robust low-dimensional quantum systems.

METHODS

Quantum-bath approach for decoherence and CCE

According to the quantum-bath theory, the spin qubit decoherence occurs because of the entanglement between the qubit and its environment⁶¹. In our spin model, the V_{B^-} spin serves as a qubit, and the main environmental degrees of freedom are the nuclear spins residing in the h-BN lattice. The nuclear spins are coupled to each other via magnetic dipolar coupling, and the nuclear spin bath interacts with the qubit through hyperfine interactions. The full spin Hamiltonian for the entire quantum many-body system is described in Supplementary Note 1. To compute the homogeneous dephasing time— T_2 —of the V_{B^-} ensembles, the Hahn-echo pulse sequence, which features a π pulse between two free evolution time τ , is considered. The decoherence of the qubit is obtained by computing the off-diagonal elements of the reduced density matrix of the qubit after tracing out the bath degrees of freedom at the end of the 2τ free evolution time, as: $\mathcal{L}(2\tau) = \frac{\text{Tr}[\rho(2\tau)S_+]}{\text{Tr}[\rho(0)S_+]}$, where S_+ is the electron

spin raising operator, and ρ is the density operator of the entire system. To compute the coherence function, we employed the CCE method^{47,62}, which systematically expands the coherence function. We find that the CCE expansion converges at the CCE-2 level of the theory, implying that the nuclear spin–spin pairwise correlation effect is the dominant source of decoherence. Extensive numerical convergence tests were performed in terms of the CCE order, bath size, and coupling radius, and the corresponding results are summarized in Supplementary Note 2 and Supplementary Fig. 1.

DFT calculations

We performed DFT calculations using plane-wave basis functions with an energy cutoff of 85 Ry, as implemented in the Quantum Espresso (QE) code⁶³ and the GIPAW module^{64,65}, to compute the nuclear quadrupole interaction and the hyperfine interaction in h-BN containing V_{B^-} with a Gaussian lattice deformation. We used the Perdew–Burke–Ernzerhof exchange–correlation functional along with the projector-augmented wave (PAW) pseudopotentials^{66,67}. To simulate an isolated V_{B^-} defect in the h-BN, we used large supercells containing either single- or multi-layer h-BN. For the single-layer h-BN calculations, we built a 336-atom supercell starting from a 4-atom orthorhombic unit cell. The h-BN layer in the supercell was separated from its periodic images in the out-of-plane direction by a 10-\AA -thick vacuum space. For the multi-layer h-BN, a 672-atom supercell was used.

To cross-check our results obtained with the orthorhombic supercell, we computed the spin Hamiltonian parameters and the V_{B^-} spin decoherence by using a 450-atom hexagonal supercell for h-BN. We show the results in Supplementary Tables 1, 2, 3, and Supplementary Figs. 8, 9 in Supplementary Information. We found that the computed EFG and hyperfine parameters obtained with the hexagonal supercell are consistent with the orthorhombic supercell results except for a few atoms near the V_{B^-} defect.

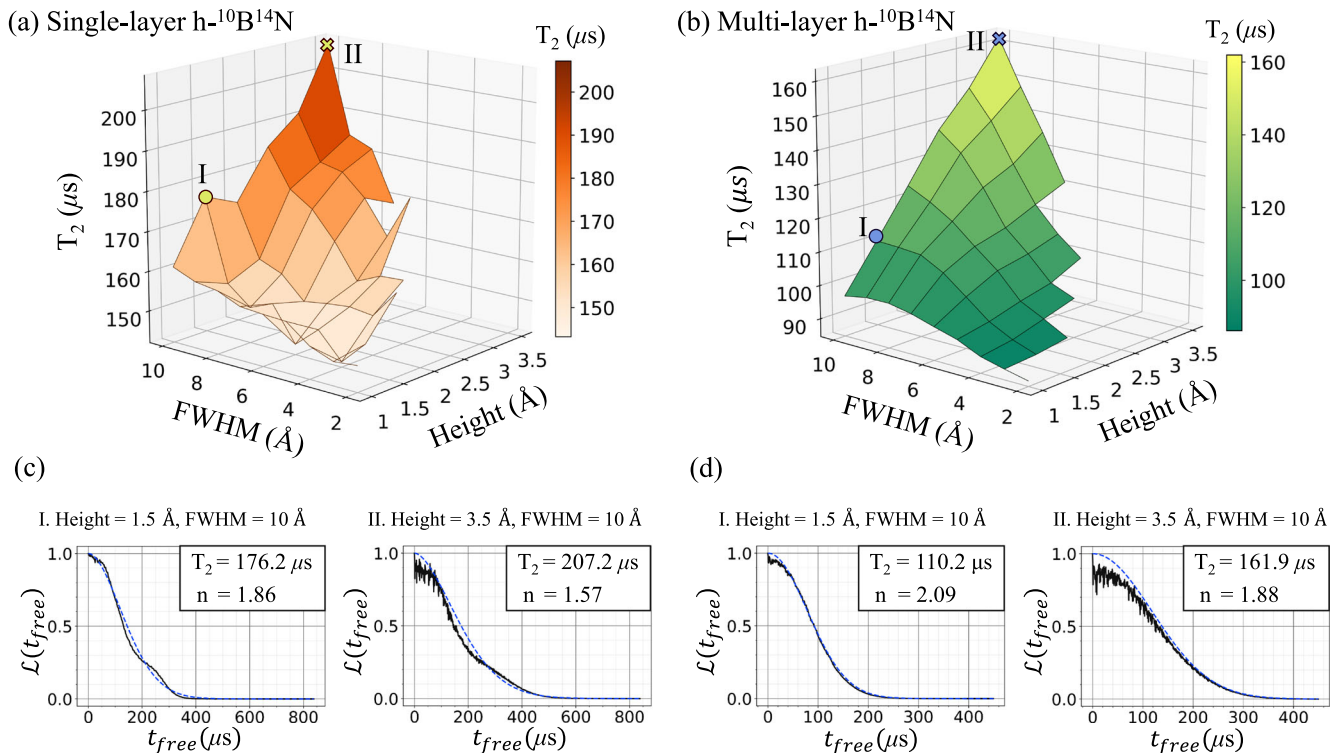


Fig. 6 Maximizing the spin coherence time of V_B^- by combining isotopic and strain engineering. **a, b** Computed T_2 of V_B^- in **a** single-layer and **b** multi-layer $\text{h-}^{10}\text{B}^{14}\text{N}$, with Gaussian lattice deformation, as a function of FWHM and height of the Gaussian deformation function. Nitrogen in the lattice is 100% ^{14}N . An external magnetic field of 3 T is applied. **c, d** V_B^- spin coherence in **c** single-layer and **d** multi-layer $\text{h-}^{10}\text{BN}$, which has a Gaussian lattice deformation corresponding to condition I (FWHM = 10 \AA and height = 1.5 \AA) and II (FWHM = 10 \AA and height = 3.5 \AA) indicated in **(a)** and **(b)**, respectively.

In particular, the EFG parameters show a noticeable difference for a few N atoms near the V_B^- due to a slight difference in the atomic relaxation depending on the supercell shape (see Supplementary Fig. 8 and Supplementary Table 2). We found, however, that this difference did not affect the main conclusion of this study. In Supplementary Fig. 9, we compare the V_B^- spin decoherence in multi-layer h-BN, computed with the orthorhombic supercell and with the hexagonal supercell. We found that the two results show only a minor difference in T_2 : 25.43 μs and 26.64 μs for the hexagonal cell and the orthorhombic cell, respectively. We remark that the sub- μs variation found in the T_2 time depending on the supercell shape does not affect the main conclusion of our study as our prediction on the T_2 enhancement in isotopically enriched h-BN and in strain-engineered h-BN is on the order of tens of μs .

DATA AVAILABILITY

The data that support the findings of this study are available upon reasonable request to the corresponding author.

CODE AVAILABILITY

The codes that were used in this study are available upon reasonable request to the corresponding author.

Received: 24 February 2022; Accepted: 24 August 2022;

Published online: 07 September 2022

REFERENCES

- Bradley, C. E. et al. A ten-qubit solid-state spin register with quantum memory up to one minute. *Phys. Rev. X* **9**, 031045 (2019).

- Barry, J. F. et al. Sensitivity optimization for NV-diamond magnetometry. *Rev. Mod. Phys.* **92**, 015004 (2020).
- Pompili, M. et al. Realization of a multinode quantum network of remote solid-state qubits. *Science* **372**, 259–264 (2021).
- Humphreys, P. C. et al. Deterministic delivery of remote entanglement on a quantum network. *Nature* **558**, 268–273 (2018).
- Doherty, M. W. et al. The nitrogen-vacancy colour centre in diamond. *Phys. Rep.* **528**, 1–45 (2013).
- Liu, G. Q., Feng, X., Wang, N., Li, Q. & Liu, R. B. Coherent quantum control of nitrogen-vacancy center spins near 1000 kelvin. *Nat. Comm.* **10**, 1344 (2019).
- Togan, E. et al. Quantum entanglement between an optical photon and a solid-state spin qubit. *Nature* **466**, 730–734 (2010).
- Weber, J. R. et al. Quantum computing with defects. *PNAS* **107**, 8513–8518 (2010).
- Atatüre, M., Englund, K., Vamivakas, N., Lee, S. Y. & Wrachtrup, J. Material platforms for spin-based photonic quantum technologies. *Nat. Rev. Mater.* **3**, 38–51 (2018).
- Zhang, G., Cheng, Y., Chou, J. P. & Gali, A. Material platforms for defect qubits and single-photon emitters. *Appl. Phys. Rev.* **7**, 031308 (2020).
- Wolfowicz, G. et al. Quantum guidelines for solid-state spin defects. *Nat. Rev. Mater.* **6**, 906–925 (2021).
- Anderson, C. P. et al. Electrical and optical control of single spins integrated in scalable semiconductor devices. *Science* **366**, 1225–1230 (2019).
- Widmann, M. et al. Electrical charge state manipulation of single silicon vacancies in a silicon carbide quantum optoelectronic device. *Nano Lett.* **19**, 7173–7180 (2019).
- Liu, X. & Hersam, M. C. 2D materials for quantum information science. *Nat. Rev. Mater.* **4**, 669–684 (2019).
- toth, M. & Aharonovich, I. Single photon sources in atomically thin materials. *Annu. Rev. Phys. Chem.* **70**, 123–142 (2019).
- Azzam, S. I., Parto, K. & Moody, G. Prospects and challenges of quantum emitters in 2D materials. *Appl. Phys. Lett.* **118**, 240502 (2021).
- Liu, Y. et al. Van der Waals heterostructures and devices. *Nat. Rev. Mater.* **1**, 16042 (2016).
- Tran, T. T., Bray, K., Ford, M. J., Toth, M. & Aharonovich, I. Quantum emission from hexagonal boron nitride monolayers. *Nat. Nanotechnol.* **11**, 37–41 (2016).

19. Gross, G. et al. Tunable and high-purity room temperature single-photon emission from atomic defects in hexagonal boron nitride. *Nat. Comm.* **8**, 705 (2017).
20. Yim, D., Yu, M., Noh, G., Lee, J. & Seo, H. Polarization and localization of single-photon emitters in hexagonal boron nitride wrinkles. *ACS Appl. Mater. Inter.* **12**, 36362–36369 (2020).
21. Noh, G. et al. Stark tuning of single-photon emitters in hexagonal boron nitride. *Nano Lett.* **18**, 4710–4715 (2018).
22. Bourrellier, R. et al. Bright UV single photon emission at point defects in h-BN. *Nano Lett.* **16**, 4317–4321 (2016).
23. Caldwell, J. D. et al. Photonics with hexagonal boron nitride. *Nat. Rev. Mater.* **4**, 552–567 (2019).
24. Exarhos, A. L., Hopper, D. A., Grote, R. R., Alkauskas, A. & Bassett, L. C. Optical signatures of quantum emitters in suspended hexagonal boron nitride. *ACS Nano* **11**, 3328–3336 (2017).
25. Dietrich, A. et al. Observation of Fourier transform limited lines in hexagonal boron nitride. *Phys. Rev. B* **98**, 081414 (2018).
26. Gottscholl, A. et al. Initialization and read-out of intrinsic spin defects in a van der Waals crystal at room temperature. *Nat. Mater.* **19**, 540–545 (2020).
27. Abdi, M., Chou, J. P., Gali, A. & Plenio, M. B. Color centers in hexagonal boron nitride monolayers: a group theory and ab initio analysis. *ACS Photonics* **5**, 1967–1976 (2018).
28. Ivády, V. et al. Ab initio theory of the negatively charged boron vacancy qubit in hexagonal boron nitride. *npj Comp. Mater.* **6**, 41 (2020).
29. Gao, X. et al. High-contrast plasmonic-enhanced shallow spin defects in hexagonal boron nitride for quantum sensing. *Nano Lett.* **21**, 7708–7714 (2021).
30. Gottscholl, A. et al. Room temperature coherent control of spin defects in hexagonal boron nitride. *Sci. Adv.* **7**, eabf3630 (2021).
31. Kianinia, M., White, S., Fröch, J. E., Bradac, C. & Aharonovich, I. Generation of spin defects in hexagonal boron nitride. *ACS Photonics* **7**, 2147–2152 (2020).
32. Gao, X. et al. Femtosecond laser writing of spin defects in hexagonal boron nitride. *ACS Photonics* **8**, 994–1000 (2021).
33. Li, C. et al. Scalable and deterministic fabrication of quantum emitter arrays from hexagonal boron nitride. *Nano Lett.* **21**, 3626–3632 (2021).
34. Gottscholl, A. et al. Spin defects in hBN as promising temperature, pressure and magnetic field quantum sensors. *Nat. Comm.* **12**, 4480 (2021).
35. Fröch, J. E. et al. Coupling hexagonal boron nitride quantum emitters to photonic crystal cavities. *ACS Nano* **14**, 7085–7091 (2020).
36. Chejanovsky, N. et al. Single-spin resonance in a van der Waals embedded paramagnetic defect. *Nat. Mater.* **20**, 1079–1084 (2021).
37. Auburger, P. & Gali, A. Towards ab initio identification of paramagnetic substitutional carbon defects in hexagonal boron nitride acting as quantum bits. *Phys. Rev. B* **104**, 075410 (2021).
38. Stern, H. L. et al. Room-temperature optically detected magnetic resonance of single defects in hexagonal boron nitride. *Nat. Comm.* **13**, 618 (2022).
39. Ye, M., Seo, H. & Galli, G. Spin coherence in two-dimensional materials. *npj Comp. Mater.* **5**, 44 (2019).
40. Anderson, C. P. et al. Five-second coherence of a single spin with single-shot readout in silicon carbide. *Sci. Adv.* **8**, eabm5912 (2022).
41. Bar-Gill, N., Pham, L. M., Jarmola, A., Budker, D. & Walsworth, R. L. Solid-state electronic spin coherence time approaching one second. *Nat. Comm.* **4**, 1743 (2013).
42. Wolfowicz, G. et al. Atomic clock transitions in silicon-based spin qubits. *Nat. Nanotechnol.* **8**, 561–564 (2013).
43. Miao, K. C. et al. Universal coherence protection in a solid-state spin qubit. *Science* **369**, 1493–1497 (2020).
44. Bhang, J., Ma, H., Yim, D., Galli, G. & Seo, H. First-principles predictions of out-of-plane group IV and V dimers as high-symmetry, high-spin defects in hexagonal boron nitride. *ACS Appl. Mater. Interfaces* **13**, 45768–45777 (2021).
45. Smart, T. J., Li, K., Xu, J. & Ping, Y. Intersystem crossing and exciton-defect coupling of spin defects in hexagonal boron nitride. *npj Comp. Mater.* **7**, 59 (2021).
46. Schweiger, A. & Jeschke, G. *Principles of Pulse Electron Paramagnetic Resonance* (Oxford Univ. Press, 2001).
47. Yang, W. & Liu, R. B. Quantum many-body theory of qubit decoherence in a finite-size spin bath. *Phys. Rev. B* **78**, 085315 (2008).
48. Seo, H. et al. Quantum decoherence dynamics of divacancy spins in silicon carbide. *Nat. Comm.* **7**, 12935 (2016).
49. Morley, G. W. et al. Quantum control of hybrid nuclear-electronic qubits. *Nat. Mater.* **12**, 103–107 (2013).
50. Witzel, W. M., Carroll, M. S., Morello, A., Cywiński, Ł. & Sarma, S. D. Electron spin decoherence in isotope-enriched silicon. *Phys. Rev. Lett.* **105**, 187602 (2010).
51. Kanai, S. et al. Generalized scaling of spin qubit coherence in over 12,000 host materials. *PNAS* **119**, e2121808119 (2022).
52. Zhao, N., Ho, S. W. & Liu, R. B. Decoherence and dynamical decoupling control of nitrogen vacancy center electron spins in nuclear spin baths. *Phys. Rev. B* **85**, 115303 (2012).
53. Slichter, C. P. *Principles of Magnetic Resonance* (Springer, 1990).
54. Maze, J. R., Taylor, J. M. & Lukin, M. D. Electron spin decoherence of single nitrogen-vacancy defects in diamond. *Phys. Rev. B* **78**, 094303 (2008).
55. Winter, M. The periodic table of the elements. <https://www.webelements.com> (2021).
56. He, L. et al. Isolating hydrogen in hexagonal boron nitride bubbles by a plasma treatment. *Nat. Comm.* **10**, 2815 (2019).
57. Liu, W. et al. An ultrastable and robust single-photon emitter in hexagonal boron nitride. *Phys. E Low. Dimens. Syst. Nanostruct.* **124**, 114251 (2020).
58. Wang, G. et al. Bending of multilayer van der Waals materials. *Phys. Rev. Lett.* **123**, 116101 (2019).
59. Vuong, T. Q. P. et al. Isotope engineering of van der Waals interactions in hexagonal boron nitride. *Nat. Mater.* **17**, 152–158 (2018).
60. He, M. et al. Phonon engineering of boron nitride via isotopic enrichment. *J. Mater. Res.* **36**, 4394–4403 (2021).
61. Breuer, H. P. & Petruccione, F. *The Theory of Open Quantum Systems* (Oxford Univ. Press, 2007).
62. Witzel, W. M. & Sarma, S. D. Quantum theory for electron spin decoherence induced by nuclear spin dynamics in semiconductor quantum computer architectures: spectral diffusion of localized electron spins in the nuclear solid-state environment. *Phys. Rev. B* **74**, 035322 (2006).
63. Giannozzi, P. et al. QUANTUM ESPRESSO: a modular and open-source software project for quantum simulations of materials. *J. Phys. Condens. Matter* **21**, 395502 (2009).
64. Yates, J. R., Pickard, C. J. & Mauri, F. Calculation of NMR chemical shifts for extended systems using ultrasoft pseudopotentials. *Phys. Rev. B* **76**, 024401 (2007).
65. Bahramy, M. S., Sluiter, M. H. F. & Kawazoe, Y. Pseudopotential hyperfine calculations through perturbative core-level polarization. *Phys. Rev. B* **76**, 035124 (2007).
66. Blöchl, P. E. Projector augmented-wave method. *Phys. Rev. B* **50**, 17953 (1994).
67. Corso, A. D. Pseudopotentials periodic table: from H to Pu. *Comput. Mater. Sci.* **95**, 337–350 (2014).
68. Lovchinsky, I. et al. Magnetic resonance spectroscopy of an atomically thin material using a single-spin qubit. *Science* **355**, 503–507 (2017).

ACKNOWLEDGEMENTS

This work was supported by the National Research Foundation of Korea (NRF) grant funded by the Korea Government (MSIT) (Nos. 2018R1C1B6008980, 2018R1A4A1024157, 2019M3E4A1078666 and 2021R1A4A1032085) and by the National Supercomputing Center with supercomputing resources including technical support (KSC-2021-CRE-0033). This work was supported by the Ajou University research fund.

AUTHOR CONTRIBUTIONS

J.L. performed the theoretical calculations. H.P. and J.L. developed the CCE code. H.S. devised and supervised the project. All authors contributed to the data analysis and production of the manuscript.

COMPETING INTERESTS

The authors declare no competing interests.

ADDITIONAL INFORMATION

Supplementary information The online version contains supplementary material available at <https://doi.org/10.1038/s41699-022-00336-2>.

Correspondence and requests for materials should be addressed to Hosung Seo.

Reprints and permission information is available at <http://www.nature.com/reprints>

Publisher's note Springer Nature remains neutral with regard to jurisdictional claims in published maps and institutional affiliations.



Open Access This article is licensed under a Creative Commons Attribution 4.0 International License, which permits use, sharing, adaptation, distribution and reproduction in any medium or format, as long as you give appropriate credit to the original author(s) and the source, provide a link to the Creative Commons license, and indicate if changes were made. The images or other third party material in this article are included in the article's Creative Commons license, unless indicated otherwise in a credit line to the material. If material is not included in the article's Creative Commons license and your intended use is not permitted by statutory regulation or exceeds the permitted use, you will need to obtain permission directly from the copyright holder. To view a copy of this license, visit <http://creativecommons.org/licenses/by/4.0/>.

© The Author(s) 2022